

Nondestructive microwave detection of a coherent quantum dynamics in cold atoms

William Dubosclard¹, Seungjin Kim¹ & Carlos L. Garrido Alzar¹  ¹

Cold atom quantum sensors based on atom interferometry are among the most accurate instruments used in fundamental physics, metrology, and foreseen for autonomous inertial navigation. However, they typically have optically complex, cumbersome, and low-bandwidth atom detection systems, limiting their practical applications. Here, we demonstrate an enabling technology for high-bandwidth, compact, and nondestructive detection of cold atoms, using microwave radiation. We measure the reflected microwave signal to coherently and distinctly detect the population of single quantum states with a bandwidth close to 30 kHz and a design destructivity that we set to 0.04%. We use a horn antenna and free-falling molasses cooled atoms in order to demonstrate the feasibility of this technique in conventional cold atom interferometers. This technology, combined with coplanar waveguides used as microwave sources, provides a basic design building block for detection in future atom chip-based compact quantum inertial sensors.

¹SYRTE, Observatoire de Paris, Université PSL, CNRS, Sorbonne Université, LNE, Paris, France. email: carlos.garrido@obspm.fr

The very last step in the measurement sequence of any cold atom quantum sensor is the detection. It amounts to the determination of the number of atoms in a given quantum state. From this information, one can compute the occupation probability of the relevant atomic states, which directly depends on the effect of the observable of interest sensed by the instrument. For instance, in atom interferometers such as state-of-the-art gyroimeters¹ and gravimeters/accelerometers^{2,3}, the phase of the interference fringes encodes the inertial forces acting upon the device. This phase is extracted from the above-mentioned occupation probability and the most widely used cold atom detection techniques to do it are destructive. Namely, resonant absorption⁴ or fluorescence imaging⁵. Although in terms of noise these techniques can be pushed to the shot-noise level limit and single-atom resolution⁶, they have serious drawbacks when considering the realization of practical and compact cold atom sensors. Indeed, after every detection event, we must produce a new cold atomic sample in a process that, in the best case, takes a few hundreds of milliseconds. As a consequence, conventional cold atom quantum sensors have a non-negligible dead-time which in turn translates into a reduced bandwidth (typically below 1 Hz) and reduced stability (far from the theoretical limit) due to the Dick effect⁷. These facts make them poorly competitive when compared to classical high bandwidth sensors.

Cold atoms in a given quantum state can also be detected nondestructively using, for example, phase-contrast imaging^{8–10}, diffraction-contrast imaging¹¹, nondestructive Faraday imaging¹², or implementing a light-matter quantum interface¹³. In particular, the latter allows one to create quantum correlations between the atoms in the sample¹⁴ and spin squeezed states¹⁵ which improve the sensor sensitivity. It also allows one to observe real-time coherent quantum dynamics¹⁶ such as Rabi oscillations. From a practical standpoint, a nondestructive detection also offers the possibility to increase the measurement bandwidth, perform multiple interrogations on the same atomic sample, reduce the sensor dead-time, and improve the sensor precision and stability. However, the above-mentioned nondestructive methods require complex optical systems and experimental set-ups, including in some cases optical cavities, to efficiently detect the light after interaction with the atoms^{17–19}. These are important limitations for the realization of practical compact cold atom quantum sensors having, for example, an atom chip as the main component of their physics package²⁰. To mitigate these limitations one possible solution is to detect the atoms nondestructively using microwave instead of light.

In typical cold atom sensors, microwave radiation is used to manipulate and modify the internal state of atoms. For instance, in microwave atomic clocks a local oscillator drives transitions between two well-defined atomic states, the clock states²¹. Using a Ramsey interrogation sequence²², the atoms initially prepared in one given clock state are transferred to the other one with a probability that depends on the difference between the microwave local oscillator frequency and the atomic frequency of the clock transition. Thus, as in other classes of cold atom interferometers such as, for example, accelerometers, gravimeters, and gyroimeters, microwave radiation is used to control the population of the relevant atomic states. However, in these devices, and in general, the back-action of the atoms on the field is always ignored.

The key element of our detection method is precisely this back-action. It plays an essential role in cavity quantum electrodynamics experiments realized in the regime of strong coupling between a cavity microwave field and single atoms²³. In these experiments, one can find and prepare the state of the cavity field by measuring the state of the atoms after interacting with the field. Complementarily, here we determine and track the quantum state of cold atoms by looking at the microwave field.

Here, we demonstrate the nondestructive microwave detection of the quantum state of cold ^{87}Rb atoms in free fall. Our detection solution is based on the fact that the microwave power radiated by an antenna into a medium depends on the radiation impedance of the medium. We first obtain the microwave spectral response of the atoms prepared in the lower $|F = 1, m_F = 0\rangle$ clock state (state 1 hereafter) by measuring the reflected microwave power as a function of the detuning to the clock transition. The obtained result is corroborated by both absorption imaging and a fit to the experimental data using the two-level atom model. We then demonstrate the nondestructive nature of our microwave detection by observing Rabi oscillations stroboscopically. We use two antennas for this measurement, alternating their interaction with the atoms. With one antenna we tilt the mean collective pseudospin by an angle of $\pi/4$ and immediately after, with the other antenna (the detection one), we find the rotation angle of the pseudospin in terms of the fractional occupation of the $|F = 2, m'_F = 0\rangle$ clock state (state 2 hereafter). Thus and so, this microwave detection technique allows us to observe Rabi oscillations on the same atomic ensemble with 0.04% of destructivity. This degree of destructivity, that tells us the percentage of population transferred to the initially unoccupied state, is estimated from the fit to the spectrum of the reflected microwave power and the 5 kHz red detuning chosen for the detection antenna.

Results

State-sensitive microwave detection. The experimental configuration and the generic timing sequence used to demonstrate our detection technique are presented in Fig. 1a. The output of a microwave source (OSC) is sent to a horn antenna via the through port of a bidirectional coupler (CPL). We then measure the reflected wave at the reverse coupled port, which is connected to a detector (D) (see Supplementary Information, Fig. S5). In this study, we used a spectrum analyzer as a power detector. However, the use of the bidirectional coupler together with a vector network analyzer allows one to get the full information, amplitude, and phase, of the reflected wave.

We start the experimental sequence shown in Fig. 1a by loading a mirror magneto-optical trap (MOT) of ^{87}Rb atoms in an atom chip. This cooling stage is followed by a molasses cooling step after which we optically pump the atoms to the hyperfine ground state $|F = 1\rangle$ (Fig. 1b). We prepare typically 10^5 atoms at $\sim 3 \mu\text{K}$ with this procedure. Thereafter, we employ different measurement protocols in the stage labeled “Microwave” in Fig. 1a, depending on the experiment to be carried out on free-falling atoms (see “Methods”). Finally, we determine the state of the atoms by absorption imaging in order to verify the outcome of the microwave state-dependent detection.

The relevant quantity that we consider in this investigation is the effective atomic reflection coefficient Γ_A . It is defined by the expression

$$\Gamma_A \equiv \frac{P_A - P_0}{P_A + P_0}, \quad (1)$$

where P_A and P_0 are respectively the reflected wave powers in the presence and absence of the cold atomic ensemble. The reflected power P_A is determined by the radiation impedance seen by the antenna and originated from the atoms (see Methods). Following the definition of Γ_A in Eq. (1), the knowledge of the absolute power is not needed, and therefore the calibration of the detector D is not required either. In Fig. 1c we show the fractional atomic population of the state 2 ($|F = 2, m'_F = 0\rangle$) as a function of the horn antenna detuning. This experimental data is extracted from the reflected microwave power and it carries the spectral signature of the

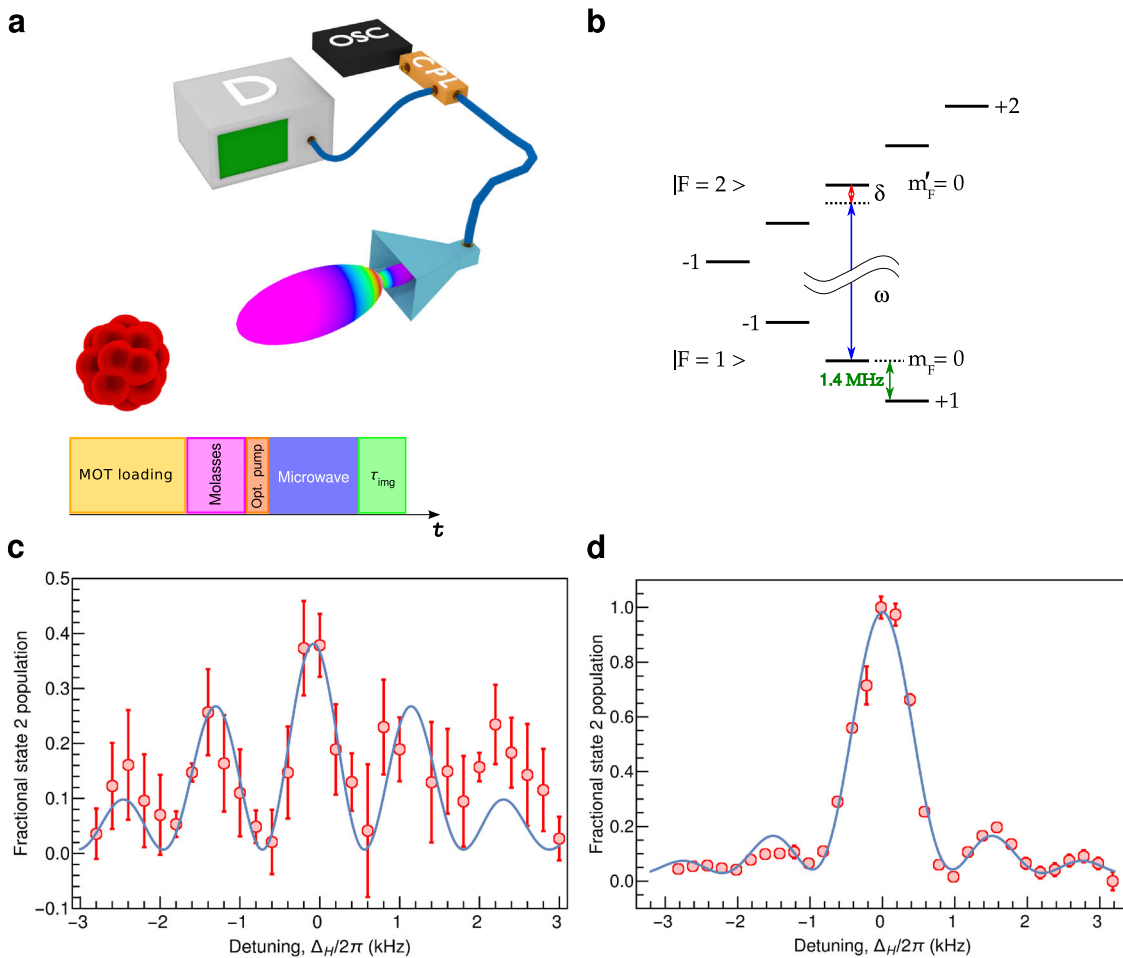


Fig. 1 Key elements of the experimental setup, timing sequence, level scheme, and level occupation probability. **a** Schematic of the experimental setup and generic timing sequence used in the measurements. The microwave generator (OSC) drives the horn antenna, used to excite and sense the atoms as represented here, through a bidirectional coupler (CPL). The atoms are detected via a modification of the antenna's radiation impedance caused by their presence. This modification is observed in the reflected microwave power picked-up at the CPL reverse coupled port and measured with a detector (D), here a spectrum analyzer in zero span mode. The step “Microwave” in the sequence corresponds to driving and/or detection of the atomic populations. **b** Relevant energy levels of the hyperfine ground states of ^{87}Rb atoms under a quantization field of 2 Gauss. The microwave at a frequency ω couples to the clock transition with an adjustable detuning. **c** Fractional state 2 population as a function of the horn detuning observed via the reflected wave power. **d** Spectrum of the fractional state 2 population as measured by absorption imaging. The blue solid lines are fits to the spectra using the two-level atom excited state population equation (see Supplementary Note 2). The error bars correspond to the standard deviation of repeated measurements.

medium in which the antenna is radiating. In our experiment, such a signature only comes from ^{87}Rb atoms. This is confirmed by the maximum signal change located at the $m_F = 0 \leftrightarrow m'_F = 0$ clock hyperfine transition frequency ($\Delta_H = 0$) driven by the horn. The state-sensitive atom detection method here introduced is fundamentally based on the observation of this spectral response in the reflected wave power.

Indeed, in typical microwave reflection measurements, the modification of the radiation resistance of an antenna by the presence of a physical system emerges as a level change in the amplitude or relative phase of the reflected wave. Specifically, when the physical system is an ensemble of cold atoms, these level modifications are weak to invisible and scale as μ_B^2/h , being μ_B the Bohr's magneton. Nevertheless, the existence of microwave atomic transitions allows one to clearly detect level variations in the weak reflected signal, as it can be seen when we scan the frequency of the applied microwave field across an atomic resonance.

To obtain the spectrum of Γ_A , the duration of the stage “Microwave” in the timing sequence (Fig. 1a) was taken equal to

that of a π pulse, which corresponds to the total transfer of the atoms from one hyperfine ground state to the other. This duration, taken equal to $980\ \mu\text{s}$, was determined from Rabi oscillations by measuring the atomic populations with the standard technique of absorption imaging (see Methods and Supplementary Information, Fig. S2). The spectrum in Fig. 1c was measured in a sub-optimal configuration because we excited and detected the atoms with the same horn antenna. For if we think of the atomic pseudospin as a realization of a qubit that will be used in a subsequent operation, then it is undesirable to modify it while it is being detected. However, it illustrates the proof-of-principle of our microwave detection technique in its simplest implementation.

Right after the application of the microwave detection pulse, we applied an absorption imaging pulse (stage “ τ_{img} ” in the timing sequence in Fig. 1a). Using this imaging pulse, we determine the atom number in state 2 and verify in this way the outcome of the microwave detection pulse. The result is presented in Fig. 1d. It shows that the data from absorption imaging is well

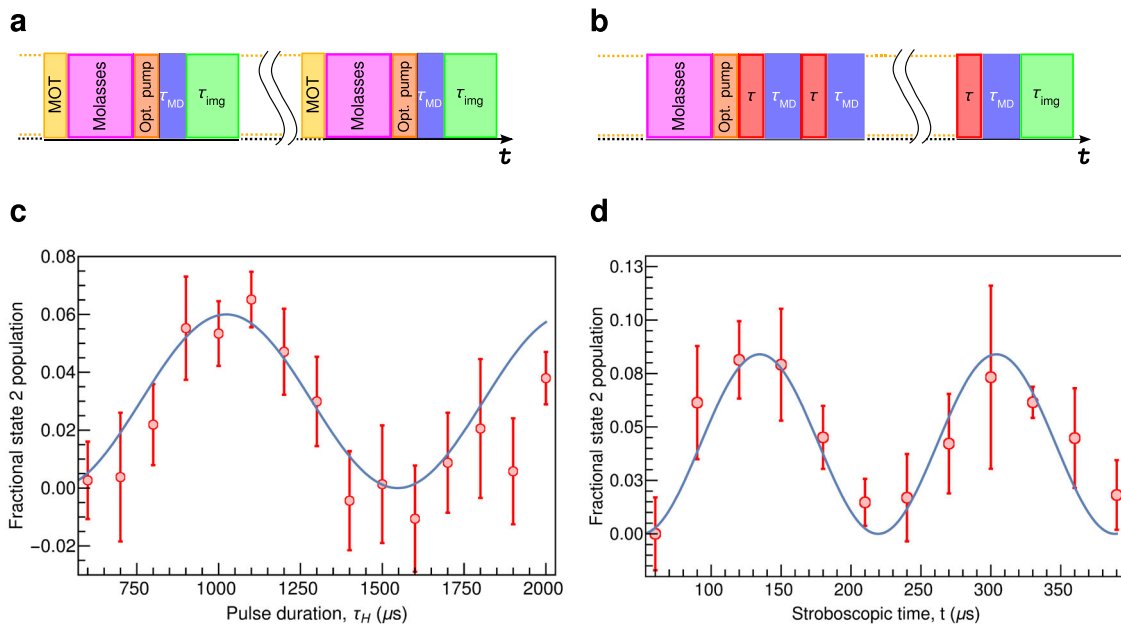


Fig. 2 Nondestructively measured Rabi oscillations. **a, b** Show respectively the timing sequences for the single-shot (horn used to drive and detect) and the stroboscopic (antenna used to drive and horn to detect) Rabi oscillation measurements. In these panels, τ_{MD} represents the duration of the microwave detection pulse done with the horn antenna. In the stroboscopic protocol in panel **(b)**, τ is the duration of the driving pulse of the dipole antenna. The duration of the absorption imaging pulse is represented by τ_{img} . Panels **c** and **d** display respectively the single-shot and the stroboscopic Rabi oscillations measured with the same initial conditions (initial atomic state). In panel **(c)**, τ_H corresponds to τ_{MD} in panel **(a)**. The stroboscopic time was varied in steps of $30\ \mu\text{s}$ for both, excitation and detection (see “Methods”). The error bars correspond to the standard deviation of repeated measurements.

correlated with the data from the microwave reflection measurement, validating this latter as a cold atom detection technique.

Nondestructive tracking of Rabi oscillations. In addition to the observed spectral sensitivity, Fig. 1c indicates that an off-resonant detection of a given atomic state population is possible with a relatively high signal-to-noise ratio. Consequently, the nondestructivity of this atom detection method is a relevant question to address. Here, we tackled this question by observing Rabi oscillations using two different measurement protocols (see “Methods”). We use two different antennas orthogonally positioned with respect to each other to implement them. In the first protocol, hereafter called single-shot, we observe Rabi oscillations by resonantly driving and simultaneously detecting the atoms with the horn antenna. The horn pulse duration τ_H is increased from one shot to the next one, and at the end of every shot we detect the atomic population in the hyperfine ground state $|F=2, m'_F=0\rangle$ by absorption imaging (see Fig. 2a). Therefore, this first protocol requires the preparation of a new cold sample every time we change the pulse duration. In the second protocol, hereafter called stroboscopic, we prepare a single cold atom sample. Then, by toggling between the driving pulse of a dipole antenna and the detection pulse of the horn (see Fig. 2b), we observe Rabi oscillations stroboscopically on the same atomic ensemble.

The Rabi oscillations observed in the single-shot configuration are presented in Fig. 2c where the fractional population data are fitted using the two-level atom model (see Supplementary Note 2). The π pulse duration obtained from the fit equals $970\ \mu\text{s}$, in agreement with the pulse duration resulting from the absorption imaging measurement (cf. Supplementary Information, Fig. S2). We show in Fig. 2d the Rabi oscillations data obtained in the stroboscopic configuration. In this case, we used a detuning of $5\ \text{kHz}$ for the horn detection pulse and adjusted its duration to

realize an equivalent π pulse (maximum probability for population transfer). The fit to the stroboscopic data in Fig. 2d reveals a π pulse duration of $120\ \mu\text{s}$, in agreement with the value measured by absorption imaging using the single-shot protocol done this time with the dipole antenna.

To observe the stroboscopic Rabi oscillations, the mean collective pseudospin was driven in steps of $\pi/4$ by the dipole antenna. As can be seen in Fig. 2d, the two Rabi fringes present the same contrast within the error bars. This fact indicates that no decoherence is introduced in this measurement by our detection technique.

Discussion

We have demonstrated in this work a state-sensitive detection technique based on the reflected power of microwave radiation in the presence of cold atoms. The core of this technique is its spectral sensitivity, shown by the effective atomic reflection coefficient of the cold atom sample. Without this spectral response, it would have not been possible to detect the atoms, contrary to other physical systems with relatively large magnetic polarizabilities or in different electromagnetic conditions^{24–27}. Indeed, the radiation impedance of an atomic ensemble is relatively small since it is determined by the magnetic polarizability which depends on the ratio μ_B^2/h^{28} . In addition to being state-sensitive, here we demonstrated that this microwave detection technique can be nondestructive. This fact is confirmed by our stroboscopic observation of Rabi oscillations between the ^{87}Rb clock states when the microwave detection frequency is chosen off-resonant from this transition. In this way, we looked at the coherent evolution of the mean collective pseudospin passing through superpositions of the two clock states. Since these superpositions are quantum by nature, then this detection technique allowed us the observation of a coherent quantum dynamics, which was confirmed by the fact that no contrast decay

was observed in the Rabi fringes obtained stroboscopically. Furthermore, via these stroboscopic measurements we demonstrated a detection bandwidth of 30 kHz, limited essentially by the available microwave power and the tolerable destructivity.

The nondestructive nature of the microwave detection here demonstrated opens a question on its application for continuous operation of cold atom interferometers^{1,29–31} and quantum state engineering^{15–19} by quantum non-demolition measurements (see Supplementary Note 3). Indeed, as shown by the stroboscopic Rabi oscillation measurement in Fig. 2, with this technique is possible to measure a superposition of quantum states without destroying it. This result suggests that, for instance, one can measure the output of a trapped atom clock or a guided atom inertial sensor, and immediately after lunch a new measurement cycle using a well-known quantum state. And, more importantly, without preparing a new cold atom sample. The direct consequence of such an operation is a reduction or suppression of the device dead-time leading to better sensor sensitivity, which in the long term translates into better sensor stability when comparing to a conventional cold atom sensor for the same integration time. We can therefore foresee, for example, inertial sensors based on complex multi-butterfly configurations and continuous clock operation.

We decided to demonstrate our detection technique using free-falling atoms because the majority of conventional cold atom interferometers work in this configuration. Besides, the use of a commercial horn antenna for detection also goes in this direction. However, its optimal realization is via coplanar waveguides in atom chips since it then provides an integrated, local, non-destructive, high-bandwidth detection of cold atoms using near field microwave radiation³². A promising solution for atom chip-based future compact cold atom quantum sensors.

Methods

Cold atom sample preparation. Our cold atom sample preparation starts with 1.5 s of loading of a standard four-laser beams mirror MOT from a rubidium vapor issue from an alkali metal dispenser (SAES RB/NF/5.4/25/FT10+10). We used a magnetic field gradient of 12 Gauss cm⁻¹, produced by in-vacuum macroscopic coils fed with 1.3 A of current. The cooling lasers were red-detuned by -1.7Γ from the $|F=2\rangle\leftrightarrow|F'=3\rangle$ D_2 line cycling transition, where $\Gamma=2\pi\times6\text{ MHz}$ is the natural linewidth of ^{87}Rb D_2 line. The four independent MOT beams, of about 2.5 cm of 1/2 diameter, shared a maximum optical power of $\approx30\text{ mW}$. After this step, we do a 40 ms transfer of the atoms to an on-chip MOT (U-MOT) by compressing the cloud with a magnetic field gradient of 20 Gauss cm⁻¹. The U-MOT was created by a micro-fabricated U-shaped wire carrying 400 mA of current. Its magnetic field combined with an external bias field of 1.75 Gauss produced a quadrupole trap with 13 Gauss cm⁻¹ of magnetic field gradient. We kept the atoms in the U-MOT during 250 ms (-3Γ red-detuned cooling lasers) before starting a 10 ms long molasses cooling step. For the molasses cooling, we red-detuned the cooling lasers by -16Γ from the cooling transition. The molasses cooling was followed by 2 ms of optical pumping that prepared a cold atom cloud at 3 μK with $\sim10^5$ atoms in the $|F=1\rangle$ hyperfine ground state. This cloud was located 300 μm from the chip surface. During the optical pumping, we used a quantization field of 2 Gauss in magnitude that we kept on in all subsequent microwave measurements.

Atomic radiation impedance. Using antenna theory³³, it can be demonstrated that an antenna emitting in the direction of an atomic sample will see a radiation impedance $Z_{\text{at}}(\mathbf{r})$ given by the equation (cf. Supplementary Note 1)

$$Z_{\text{at}}(\mathbf{r}) = \gamma R_{\text{rad}} 6\pi \frac{\omega^2}{k^3} \beta_m(\omega) \mathcal{H}_m^2(\mathbf{r}), \quad (2)$$

where R_{rad} , ω , k , $\beta_m(\omega)$, and $\mathcal{H}_m(\mathbf{r})$ are respectively the antenna's radiation resistance in the absence of the atomic sample, the frequency and wave vector of the emitted electromagnetic radiation, the magnetic polarizability of the atoms, and the position-dependent amplitude of the magnetic field radiated per atomic magnetic dipole in a unit of time. Here, γ denotes the imaginary unit and \mathbf{r} is the radius vector between the antenna and an atom in the cloud. To arrive at Eq. (2) we have considered that the magnetic field component of the microwave radiation of the antenna excites the magnetic dipole of the atoms, which in turn radiates a microwave field picked up by the antenna.

Atomic magnetic polarizability. The magnetic polarizability, on its part, is determined by the atomic transitions n with a frequency near to the one radiated by the antenna. In general, it is a tensor given by the equation²⁸

$$\beta_{ij}^{(n)}(\omega) = \mu_0 \frac{\mu_i^{ab(n)} \mu_j^{ba(n)}}{\hbar} \frac{2a_{ba}^{(n)}}{(\omega_{ba}^{(n)})^2 - \omega^2 + j\gamma\omega}, \quad (3)$$

where μ_0 is the vacuum magnetic permeability, n identifies a particular transition, $i, j = x, y, z$ indicate the direction in space, a and b stands for the initial $|a\rangle$ and final $|b\rangle$ states of the considered transition with matrix element $\mu_i^{ab(n)}$ in the i direction, and γ is a phenomenological decay constant. For instance, in the case of isotropic polarizability we will have

$$\beta_m(\omega) = \frac{1}{3} \sum_n \sum_{i=x,y,z} \beta_{ii}^{(n)}(\omega), \quad (4)$$

with

$$\beta_{ii}^{(n)}(\omega) = \mu_0 \frac{|\mu_i^{ab(n)}|^2}{\hbar} \frac{2\omega_{ba}^{(n)}}{(\omega_{ba}^{(n)})^2 - \omega^2 + j\gamma\omega}. \quad (5)$$

Atomic microwave reflection coefficient. The atomic reflection coefficient $\Gamma_{\text{at}}(\mathbf{r})$ can be defined in terms of the radiation impedance of the atoms as

$$\Gamma_{\text{at}}(\mathbf{r}) \equiv \frac{Z_{\text{at}}(\mathbf{r}) - R_{\text{rad}}}{Z_{\text{at}}(\mathbf{r}) + R_{\text{rad}}}. \quad (6)$$

In our setup, the emitting element of the horn antenna is at $r_{\text{at}} \approx 8.4\text{ cm}$ from the initial cloud position and therefore, $kr_{\text{at}} \approx 12 \gg 1$. This condition implies that it is appropriate to use the far-field approximation for $\mathcal{H}_m(\mathbf{r})$ to get an order of magnitude of $\Gamma_{\text{at}}(\mathbf{r})$ and its dependence on the microwave radiation frequency. In the far-field situation, the amplitude of the magnetic field radiated per atomic magnetic dipole per second is given by $\mathcal{H}_m(\mathbf{r}) = \omega \sin(\theta)/4\pi c^2 r$, where c has the usual meaning, θ is the polar angle and r is the distance between the antenna and the atomic sample.

Time-of-flight atomic impedance of a finite temperature atomic cloud. For an atom cloud free falling in the y direction, the atomic microwave reflection coefficient is determined by the time-of-flight atomic impedance $Z_{\text{atTOF}}(t)$, which is given by the equation

$$Z_{\text{atTOF}}(t) = \frac{1}{(2\pi\sigma_t^2)^{3/2}} \int d^3\mathbf{r} Z_{\text{at}}(\mathbf{r}) \exp\left[-\frac{x^2}{2\sigma_t^2} - \frac{(y - gt^2/2)^2}{2\sigma_t^2} - \frac{z^2}{2\sigma_t^2}\right], \quad (7)$$

where we have considered a Gaussian position probability density function of the atoms in the cloud, being $\sigma_t^2 \equiv \sigma_0^2 + (k_B T/M)^2 t^2$ the cloud size at a time instant t . Here, σ_0 , k_B , T , and M are respectively the initial cloud size, the Boltzmann's constant, the cloud temperature, and the mass of a ^{87}Rb atom. The use of the far-field approximation for the amplitude of the magnetic field radiated per atomic magnetic dipole in a unit of time leads to a Gaussian integral of a rational function in Eq. (7). This integral can be calculated analytically³⁴ and we obtain for the time-of-flight atomic impedance the result

$$Z_{\text{atTOF}}(t) = \gamma \frac{3}{8\pi} \frac{1}{(2\pi\sigma_t^2)^{3/2}} R_{\text{rad}} k \beta_m(\omega) \lim_{\zeta \rightarrow 0} F_\zeta(\sigma_t), \quad (8)$$

where the function $F_\zeta(\sigma_t)$ has the form

$$F_\zeta(\sigma_t) = \pi^{3/2} \zeta^{1/2} \left\{ \frac{1}{2} \Gamma(-1/2, \zeta/2\sigma_t^2) \left[1 + \frac{g^2(t^2 - t_0^2)^2}{4\sigma_t^2} \right] \right. \\ \left. + \frac{\zeta}{4\sigma_t^2} \Gamma(-3/2, \zeta/2\sigma_t^2) - \zeta^{-1} \frac{g^2(t^2 - t_0^2)^2}{4} \Gamma(1/2, \zeta/2\sigma_t^2) \right\} \exp(\zeta/2\sigma_t^2). \quad (9)$$

In Eq. (9), $\Gamma(\cdot)$ is the upper incomplete Gamma function and t_0 is the time required for an atom to reach the H-plane of the horn antenna, starting from the initial position $y = 0$ (see Supplementary Methods).

Rabi oscillations observed with absorption imaging. After preparing the atoms in the $|F=1, m_F=0\rangle$ state, we applied a microwave pulse using the horn to drive the $|F=1, m_F=0\rangle\leftrightarrow|F=2, m_F'=0\rangle$ clock transition. We varied the duration τ_H of this pulse (stage "Microwave" in the timing sequence in Fig. 1a) and measured the atom number in the state $|F=2, m_F'=0\rangle$ using absorption imaging (stage " t_{img} " in Fig. 1a). We obtained the Rabi oscillation shown in Supplementary Information Fig. S2, where every point and its corresponding error bar result from 9 realizations with very similar if not the same experimental conditions. From the Supplementary Information Fig. S2 we find a duration of the π pulse (980 μs) used in all the microwave reflection measurements, except for the stroboscopic Rabi oscillations.

Fractional state 2 population. To find the fractional state 2 population, we fit a Lorentzian to the central region of the effective atomic reflection coefficient spectrum (see Supplementary Information, Fig. S3). Then, we compute the fractional state 2 population using the peak Γ_{Apk} and the baseline Γ_{Ab} values extracted from this fit. The formula used to do this calculation is

$$\frac{\Gamma_{\text{A}} - \Gamma_{\text{Ab}}}{\Gamma_{\text{Apk}} - \Gamma_{\text{Ab}}}. \quad (10)$$

Single-shot Rabi oscillations observed by microwave reflection. In the single-shot protocol (Fig. 2a), we prepare a cold atom sample in the initial state $|F = 1, m_F = 0\rangle$ as explained in the main text (see timing sequence in Fig. 1a). Then, we apply a resonant microwave pulse of a fixed duration τ_{H} with a horn antenna. Finally, we detect the atom number in the state $|F = 2, m_F' = 0\rangle$ using absorption imaging. Starting from the cooling of a new sample, these steps are repeated increasing the driving pulse duration τ_{H} .

Stroboscopic Rabi oscillations observed by microwave reflection. In the stroboscopic protocol we use two antennas, a horn and a dipole one. The protocol starts with the preparation of a cold atom sample in the initial state $|F = 1, m_F = 0\rangle$. Then, we apply a driving resonant pulse with the dipole antenna. This dipole antenna is placed at 90° with respect to the emission direction of the horn. We chose for this pulse a duration corresponding to a $\pi/4$ pulse. Subsequently, using the horn, we apply a microwave off-resonant detection pulse with a duration corresponding to its π pulse. The driving and detection pulses are then toggled (see Fig. 2b) in order to track the Rabi oscillation on the same cold atom sample. In this measurement protocol, the polarization of the magnetic field of the horn is chosen parallel to the homogeneous field setting the quantization axis. Consequently, during the detection pulse, the horn magnetic field just modulates the magnitude of the quantization field with a low modulation depth of 0.7×10^{-3} ($\approx 1 \text{ kHz}/1.4 \text{ MHz}$).

Microwave sources. We use two microwave generators (SynthHD PRO: 54 MHz - 13.6 GHz Dual Channel Microwave Generator) from Windfreak Technologies LLC to drive the horn and the dipole antennas. Despite their versatility, we must point out that care must be taken when switching on or pulsing these generators. They have a turn-on power transient (actual power higher than the setting) that lasts around 90 μs (cf. Supplementary Information, Fig. S4). After this time interval, the actual power stabilizes to the requested one. Therefore, when measuring Rabi oscillations by changing the pulse duration, the data inside this turn-on transient window will correspond to a higher Rabi frequency than the desired one. We considered this fact by excluding the data inside this window by properly designing the data acquisition and data treatment. The schematic diagram of the experimental setup used to detect the atomic signals is shown in Supplementary Information, Fig. S5.

Data and materials availability

All data needed to evaluate the conclusions are present in the paper and/or in the Supplementary Information. Additional data related to this paper may be requested from the authors.

Received: 1 October 2020; Accepted: 1 February 2021;

Published online: 24 February 2021

References

1. Savoie, D. et al. Interleaved atom interferometry for high sensitivity inertial measurements. *Sci. Adv.* **4**, eaau7948 (2018).
2. Gillot, P., Francis, O., Landragin, A., Pereira Dos Santos, F. & Merlet, S. Stability comparison of two absolute gravimeters: optical versus atomic interferometers. *Metrologia* **51**, L15 (2014).
3. Zhou, M.-K. et al. Micro-Gal level gravity measurements with cold atom interferometry. *Chin. Phys. B* **24**, 050401 (2015).
4. Bose-Einstein Condensation in Atomic Gases, in *Proceedings of the International School of Physics "Enrico Fermi"*, Course CXL (eds Inguscio, M., Stringari, S. & Wieman, C.) (Amsterdam and IOS Press, 1999).
5. Hu, Z. & Kimble, H. J. Observation of a single atom in a magneto-optical trap. *Opt. Lett.* **19**, 1888 (1994).
6. Gajdacz, M. et al. Preparation of ultracold atom clouds at the shot noise level. *Phys. Rev. Lett.* **117**, 073604 (2016).
7. Dick, G. J. Local oscillator induced instabilities, in *Proceedings of the 19th Annual Precise Time and Time Interval (PTTI) Applications and Planning Meeting*, Redondo Beach, CA, (1987).
8. Andrews, M. R. et al. Direct, nondestructive observation of a bose condensate. *Science* **273**, 84 (1996).
9. Andrews M. R. et al. Propagation of sound in a Bose-Einstein condensate. *Phys. Rev. Lett.* **79**, 553 (1997); Erratum *Phys. Rev. Lett.* **80**, 2967 (1998).
10. Higbie, J. M. et al. Direct nondestructive imaging of magnetization in a spin-1 Bose-Einstein gas. *Phys. Rev. Lett.* **95**, 050401 (2005).
11. Turner, L. D., Domen, K. F. E. M. & Scholten, R. E. Diffraction-contrast imaging of cold atoms. *Phys. Rev. A* **72**, 031403(R) (2005).
12. Gajdacz, M. et al. Non-destructive Faraday imaging of dynamically controlled ultracold atoms. *Rev. Sci. Instrum.* **84**, 083105 (2013).
13. Hammerer, K., Sørensen, A. S. & Polzik, E. S. Quantum interface between light and atomic ensembles. *Rev. Mod. Phys.* **82**, 1041 (2010).
14. Julsgaard, B., Kozhekin, A. & Polzik, E. S. Experimental long-lived entanglement of two macroscopic objects. *Nature* **413**, 400 (2001).
15. Appel, J. et al. Mesoscopic atomic entanglement for precision measurements beyond the standard quantum limit. *Proc. Natl Acad. Sci. USA* **106**, 10960 (2009).
16. Windpassinger, P. J. et al. Nondestructive probing of rabi oscillations on the cesium clock transition near the standard quantum limit. *Phys. Rev. Lett.* **100**, 103601 (2008).
17. Leroux, I. D., Schleier-Smith, M. H. & Vuletić, V. Implementation of cavity squeezing of a collective atomic spin. *Phys. Rev. Lett.* **104**, 073602 (2010).
18. Hosten, O., Engelsen, N. J., Krishnakumar, R. & Kasevich, M. A. Measurement noise 100 times lower than the quantum-projection limit using entangled atoms. *Nature* **529**, 505 (2016).
19. Huang, M.-Z. et al. Self-amplifying spin measurement in a long-lived spin-squeezed state. <http://arxiv.org/abs/2007.01964> (2020).
20. Garrido Alzar, C. L. Compact chip-scale guided cold atom gyroimeters for inertial navigation: Enabling technologies and design study. *AVS Quantum Sci.* **1**, 014702 (2019).
21. Bize, S. et al. Cold atom clocks and applications. *J. Phys. B: Mol. Opt. Phys.* **38**, S449 (2005).
22. Ramsey, N. F. History of atomic clocks. *Bur. Stand.* **88**, 301 (1983).
23. Haroche, S. Nobel lecture: controlling photons in a box and exploring the quantum to classical boundary. *Rev. Mod. Phys.* **85**, 1083 (2013).
24. Takeda, S. & Tsukishima, T. *Microwave Reflection Techniques for Dense Plasma Diagnostics* (U.S. Department of Commerce, National Bureau of Standards, 1965).
25. Slobozhanyuk, A. P., Poddubny, A. N., Krasnok, A. E. & Belov, P. A. Magnetic Purcell factor in wire metamaterials. *Appl. Phys. Lett.* **104**, 161105 (2014).
26. Krasnok, A. E. et al. An antenna model for the Purcell effect. *Sci. Rep.* **5**, 12956 (2015).
27. Funk, D. B., Gillay, Z. & Meszaros, P. Unified moisture algorithm for improved RF dielectric grain moisture measurement. *Meas. Sci. Technol.* **18**, 1004 (2007).
28. Haakh, H. et al. Temperature dependence of the magnetic Casimir-Polder interaction. *Phys. Rev. A* **80**, 062905 (2009).
29. Dutta, I. et al. Continuous cold-atom inertial sensor with 1 nrad/sec rotation stability. *Phys. Rev. Lett.* **116**, 183003 (2016).
30. McGuinness, H. J., Rakholia, A. V. & Biedermann, G. W. High data-rate atom interferometer for measuring acceleration. *Appl. Phys. Lett.* **100**, 011106 (2012).
31. Shiga, N. & Takeuchi, M. Locking the local oscillator phase to the atomic phase via weak measurement. *N. J. Phys.* **14**, 023034 (2012).
32. Garrido Alzar, C. L. FR patent pending, FR2006563 (2020).
33. Balanis, C. A. *Antenna theory: analysis and design* (Wiley, New Jersey, ed. 3, 2005).
34. <https://math.stackexchange.com/q/3004848>, Mathematics Stack Exchange.

Acknowledgements

This work was supported by the Délégation Générale de l'Armement (DGA) through the ANR ASTRID program under grants nos. ANR-13-ASTR-0031-01, ANR-18-ASMA-0007-01, and by the Institut Francilien de Recherche sur les Atomes Froids (IFRAF). WD acknowledges funding from the Délégation Générale de l'Armement under grant no. 2017600047. We acknowledge C. Chaumont and B. Faouzi from GEPI for assistance with the atom chip fabrication. Commercial products are cited to help in the repeatability of the experiments and are not an endorsement of the related companies.

Author contributions

C.L.G.A. developed the theory, conceived and designed the experiment. W.D., S.K., and C.L.G.A. implemented the experiment. W.D. and S.K. performed the calibrations and preliminary tests. W.D. collected and processed the presented experimental data under the supervision of C.L.G.A., W.D., and C.L.G.A. carried out the data analysis and interpretation. C.L.G.A. wrote the manuscript. All authors discussed the manuscript.

Competing interests

The authors declare no competing interests.

Additional information

Supplementary information The online version contains supplementary material available at <https://doi.org/10.1038/s42005-021-00541-3>.

Correspondence and requests for materials should be addressed to C.L.G.A.

Reprints and permission information is available at <http://www.nature.com/reprints>

Publisher's note Springer Nature remains neutral with regard to jurisdictional claims in published maps and institutional affiliations.



Open Access This article is licensed under a Creative Commons Attribution 4.0 International License, which permits use, sharing, adaptation, distribution and reproduction in any medium or format, as long as you give appropriate credit to the original author(s) and the source, provide a link to the Creative Commons license, and indicate if changes were made. The images or other third party material in this article are included in the article's Creative Commons license, unless indicated otherwise in a credit line to the material. If material is not included in the article's Creative Commons license and your intended use is not permitted by statutory regulation or exceeds the permitted use, you will need to obtain permission directly from the copyright holder. To view a copy of this license, visit <http://creativecommons.org/licenses/by/4.0/>.

© The Author(s) 2021